World Electric Vehicle Journal

MDPI

Article

Multi-Strategical Thermal Management Approach for Lithium-Ion Batteries: Combining Forced Convection, Mist Cooling, Air Flow Improvisers and Additives

Anikrishnan Mohanan and Kannan Chidambaram *

School of Mechanical Engineering, Vellore Institute of Technology, Vellore 632014, India; anikrishnan.m@vit.ac.in
* Correspondence: kannan.chidambaram@vit.ac.in

Abstract: Maintaining the peak temperature of a battery within limits is a mandate for the safer operation of electric vehicles. In two-wheeler electric vehicles, the options available for the battery thermal management system are minuscule due to the restrictions imposed by factors like weight, cost, availability, performance, and load. In this study, a multi-strategical cooling approach of forced convection and mist cooling over a single-cell 21,700 lithium-ion battery working under the condition of 4C is proposed. The chosen levels for air velocities (10, 15, 20 and 25 m/s) imitate real-world riding conditions, and for mist cooling implementation, injection pressure with three levels (3, 7 and 14 bar) is considered. The ANSYS fluent simulation is carried out using the volume of fluid in the discrete phase modelling transition using water mist as a working fluid. Initial breakup is considered for more accurate calculations. The battery's state of health (SOH) is determined using PYTHON by adopting the Newton–Raphson estimation. The maximum temperature reduction potential by employing an airflow improviser (AFI) and additives (Tween 80, 1-heptanol, APG0810, Tween 20 and FS3100) is also explored. The simulation results revealed that an additional reduction of about 11% was possible by incorporating additives and AFI in the multi-strategical approach. The corresponding SOH improvement was about 2%. When the electric two-wheeler operated under 4C, the optimal condition (Max. SOH and Min. peak cell temp.) was achieved at an air velocity of 25 m/s, injection pressure of 7 bar with AFI and 3% (by wt.) Tween 80 and a 0.1% deformer.

Keywords: battery thermal management; forced convection; mist cooling; airflow improviser; additives; multi-strategical cooling; temperature attenuation; SOH

Citation: Mohanan, A.; Chidambaram, K. Multi-Strategical Thermal Management Approach for Lithium-Ion Batteries: Combining Forced Convection, Mist Cooling, Air Flow Improvisers and Additives. *World Electr. Veh. J.* **2024**, *15*, 213. https://doi.org/10.3390/wevj15050213

Academic Editors: Chengjiang Li and Xin Zou

Received: 18 April 2024
Revised: 8 May 2024
Accepted: 10 May 2024
Published: 11 May 2024

1. Introduction

The effective battery thermal management system (BTMS) is essential in all applications, and every automotive industry's primary focus has been shifted towards this domain with the boosted-up sale of electric vehicles (EV). Electric vehicles invariably use lithium-ion (Li-ion) batteries due to high energy density, lower self-discharge and a longer cycle life. However, extreme temperatures can cause Li-ion batteries to lose their performance and pose safety hazards. Thus, BTMS is essential to keep the battery temperatures within safe limits. For this purpose, several automakers use passive cooling techniques, such as phase change materials or sophisticated thermal insulating materials, to improve heat dissipation and reduce temperature swings. Despite their effectiveness, these methods have inherent drawbacks of being heavier and more complex.

Some of the new state-of-the-art systems that have been developed to address this issue include hybrid systems using forced, liquid cooling PCMs and heat pipes have also been explored. Systems have air cooling as a popular method, which increases the power-to-dimension ratio and reduces the size of both synchronous and asynchronous motors along with liquid cooling systems, which can achieve up to 25 kW/kg; however, they need strong ingress protection ratings that have been equally explored with variations in

materials, fluids and the methodology of application. This study exposes the specificity and disadvantages of the use of said systems elsewhere [1–4].

In electric two-wheelers, forced convection is dominantly used for cooling purposes. A sudden surge in power demand can make the propulsion batteries subject to high discharge rates and proportionally higher heat generation rates. This, in turn, increases the chances of thermal runaway and presents serious safety concerns. To prevent this, EV manufacturers started the implementation of alternate strategies, including multi-strategical approaches and design alterations. A review of battery thermal management suggested the approaches viz. mist cooling, nanofluid cooling, phase change material (PCM), heat pipes and other existing methods can be effectively utilised for cooling the batteries [5]. The positive influence of design alterations by employing fins, ducts, vents, air flow improvisers and possible variations in the arrangement of cells [6–8] have also been explored both numerically and experimentally.

Mist cooling, especially water-based, can remove about 65% of the battery heat build-up while maintaining outstanding performance. A numerical simulation work [9], which compared the performance of mist cooling, and traditional air cooling revealed that the battery surface temperature can be kept below 40 °C by adapting an optimal mist flow rate and air velocity. Nevertheless, efficiency is reduced by the droplet's retention time at high temperatures. This study also disclosed that an inhomogeneous cooling mechanism in the form of fine water mist could eradicate thermal runaway (TR) risks. For further effectiveness of melioration, other possible materials than water could also be employed. For TR mitigation in Li-ion batteries, experimental research that combines the porous material with water mist has also been explored [10]. The dependence upon any BTMS can be evaluated using failure mode effects analysis (FMEA), which assesses the reliability of various inhibitory strategies. The results demonstrated a good suppression effect, which was achieved through pre-insulation and heat dissipation. The synergistic inhibitory effect exhibited by the fine water mist and porous material was excellent, and a 46% increase in cooling efficiency was reported over air cooling. The temperature rise, which characterises the cooling system's hazard control impact, is guided by a conservative temperature of 240 °C.

Droplet size, fluid properties, fan speed, injection pressure and spray angle are some variables that control the effectiveness of multi-strategical approaches like mist cooling with forced convection. The change in droplet size can be attained by changing the spray pressure or injection pressure. The impact of different droplet sizes was experimentally studied using a water mist control technique [11,12]. The authors concluded that water mist with heterogeneous particle sizes substantially lowered the battery's peak temperature while simultaneously reducing the cooling period. In addition, this approach improved the water utilisation rate when compared to water mist of identical size. The effectiveness of mist cooling is also influenced by the initial temperature. In an experimental study [13], the authors explored the cooling effect of water mist by running numerous experiments on Li-ion batteries at varying initial temperatures (106–206 °C) with and without water mist. The experimental results evidenced that TR prevention caused a considerable reduction in battery failure via the presence of water mist. Moreover, the temperature of a cell experiencing TR must be lowered to below 126 °C to use water mist. The literature has disclosed that changes in injection pressure and injection quantity cause substantial changes in cooling effectiveness with water mist. It is established that water mist has an outstanding cooling capability to stop TR propagation by merely consuming 1.95×10^{-4} kg Wh^{-1} of water. The surface temperature was reduced to 100.15 °C in a fraction of a second, and the highest cooling rate exceeding 100 °C s^{-1} was achieved in Li-ion batteries with water mist. Thus, the injection rate, injection timing and frequency can be taken as control variables to dictate the cooling magnitude in water mist-based strategies. The choice of fluids and the ratio of additives in the base fluid also possess an important role in cooling as the heat transfer rate is directly correlated to the fluid's heat transfer coefficient and other physical parameters.

The ever-increasing demand for more power in EVs places the Li-ion batteries subject to thermal risks. It is essential to keep the battery temperature within safe limits to mitigate the thermal runaway. From this perspective, several studies have been conducted to attenuate the maximum cell temperature by adopting different strategies. The author explored such research works to construct a basic building block for study gap identification and its importance [14–20]. However, to the best of the author's knowledge, there are few or no studies that execute a detailed exploration of the impact of inlet velocities and injection pressure using a multi-strategical cooling approach, especially under the high charge/discharge rate (~4C) of batteries. Thus, the objectives of this present work were formulated as (i) investigating the impact of stand-alone air cooling with different air velocities, (ii) enquiring into the influence of mist cooling with different injection pressures, (iii) exploring the combined impact of air velocities and injection pressures in the combinational cooling approach, and (iv) examining the effect of mists generated by different fluids.

2. Materials and Methods

The 3D model of a 21,700 lithium-ion battery cell encompassing exact dimensions and material qualities was modelled using the 2023 R2 ANSYS design modeller. To accurately simulate airflow and mist injection dynamics, a computational domain was created, which included a control volume enclosing the battery cell. With careful refinement, a tetrahedral mesh structure was used around critical locations, such as the battery surface and injector. This was carried out to ensure precision and to capture the intricate boundary layer phenomenon, which has a significant influence on heat dissipation. Extensive mesh independence research was conducted to guarantee robustness and independence from the chosen mesh size and eliminate any chance of numerical inaccuracies. A transient, incompressible, turbulent flow model available in ANSYS Fluent was adopted in this research to solve the governing equations for fluid flow and heat transport processes. The turbulence effects in the flow domain are represented by the well-known k-epsilon turbulence model. When addressing the heat generation that results from electrochemical processes within the battery, latent heat related to mist evaporation is considered and incorporated into the energy equations. Figure 1 shows the battery specification, control volume design, properties and assumption of simulation. The specifications and boundary conditions of the simulation are presented in Table 1.

Table 1. Specifications and boundary conditions of the simulation.

Part Name/Properties	Specification	Values			
Nozzle	PJ10 (Mist cooling)	-			
Simulation runtime	seconds	120			
Injection pressure	-	3.5	7	14	-
Inlet air velocity	m/s	10	15	20	25
C-rating	-	4C			
Simulation model	Volume of Fluid to Discrete phase modelling				

The coupled solver with the energy equation was used to simulate the assumed condition of 100% SOC of the battery. The volume of the fluid to discrete phase modelling was employed to generate the flow through the nozzle. The turbulence caused by the airflow and mist was taken into consideration using the k-epsilon turbulence model. The simulation continued until a steady-state solution was achieved for every combination of convection velocities and mist injection rates. A well-established Ranz–Marshall correlation model was considered to account for the latent heat effect and its contribution to heat dissipation. The momentum, energy, and turbulence equations were discretised using second-order methods. The battery cell was placed inside a rectangular control volume (0.1 m × 0.06 m × 0.09 m) representing the air domain and at 0.50 m from the inlet. To

ensure a converged solution and reliable numerical results, strict convergence criteria were set for the residuals of all variables. The boundary conditions set for the control volume are presented below for the turbulence model.

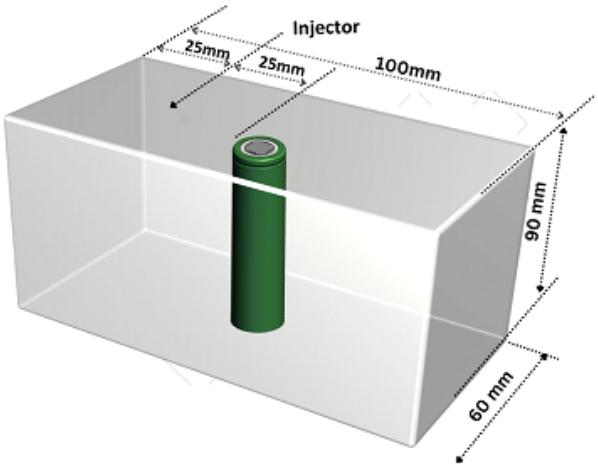

Assumptions

- The walls are adiabatic.
- Gravity is considered.
- The flow is turbulent.
- Primary breakup, secondary breakup and children of secondary breakup are considered.
- Between the mist particles and the cell surface, heat transmission takes place

Battery Specifications	Air Properties	Water Properties
Battery type: 21700 lithium-ion	Density: 1.225 kg/m3	Density: 998 kg/m3
Dimensions: 21.25 mm dia, 70.08 mm length	Viscosity: 1.7894 x 10^{-5} kg/ms	Specific heat: 4182 J/kgK
Nominal capacity: 5000 mAh	Specific heat: 1006 J/kgK	Latent heat of vaporization:
Chemistry:LiNiMnCoO2 (NMC)	Viscosity: 0.001003 kg/ms	2257 kJ/kg
Energy Density: 270 Wh/kg	Thermal conductivity: 0.0242 W/mK	

Figure 1. Design specifications, boundary conditions and assumptions for simulation.

The inlet and outlet faces were assigned a velocity inlet and a pressure outlet, respectively, with varying air velocities of 0, 15, 20 and 25 m/s.

The top face was assigned as the mist cooling condition, with varying water injection pressures of 3.5, 7 and 14 bar (selection was conducted based on the injector datasheet [21])

A circular nozzle with a diameter of 0.001 m was located at the top centre of the control volume.

The bottom and side faces were assigned a wall condition, with a constant temperature of 25 °C and a no-slip condition.

The mesh for the computational domain was generated using ANSYS Meshing, with a mesh size of 0.001 m, resulting in a total of about 8, 45, 232 elements. The simulation was made to run for 120 s, with a time step of 0.01 s. The convergence criteria for the residuals were set to 1×10^{-6} for all equations. The heat flux and heat generation rate were calculated.

The following basic equations were adopted during the simulation procedure.

Continuity equation:

$$\nabla \cdot V = 0 \tag{1}$$

Momentum equation:

$$\rho_f (V \cdot \nabla) V = \nabla P + \mu_f \nabla^2 V \tag{2}$$

Energy equation:

$$\rho_f C_{pf} \left(\frac{\partial T_f}{\partial T} \right) + \rho_f C_{pf} \left(V \cdot \nabla T_f \right) = k_f \nabla^2 T_f \tag{3}$$

where V—fluid velocity (m/s), ρ is the fluid density (kg/m^3), μ_f is the fluid dynamic viscosity (kg/ms), C_{pf} is the fluid's specific heat (J/KgK), T_f is the fluid's temperature (°C), k_f is the fluid's thermal conductivity (W/mK), and air is the working fluid.

The production of heat from batteries is a complex process that is dependent on the electrochemical characteristics of the battery, which are influenced by the ambient temperature, state of charge, and charge/discharge rates. The total heat generated is the product of reversible heat (entropic changes) and irreversible heat (enthalpy changes).

$$Q_{total} = Q_{reversible} + Q_{Irreversible} \tag{4}$$

$$Q_{irreversible} = I^2R \tag{5}$$

where I—current and R—resistance

$$Q_{Reversible} = -IT\left(\frac{\nabla S}{nF}\right),\ \nabla S = nF\left(\frac{\partial E}{\partial T}\right) \tag{6}$$

where n—number of electrons; F—Faraday's constant (C·mol^{-1}).

$$Q_{total} = I^2R - IT\left(\frac{\partial E}{\partial T}\right) \tag{7}$$

or

$$Q_{total} = I\left(V_{open\ circuit\ voltage} - V_{battery\ terminal}\right) - IT\left(\frac{\partial V_{open\ circuit}}{\partial T}\right) \tag{8}$$

where I—current (amp), R—resistance (ohm), and T—temperature (°C).

Since this work mainly focuses on mist cooling, water droplets of varying sizes (10 µm to 100 µm) should be considered depending on the breakup and its results. The species transport equation shown in Equation (10) was utilised to solve the problem.

$$\frac{\partial(\rho Y_{vapour})}{\partial t} + \nabla\cdot(\rho u Y_{vapour}) = \nabla\cdot(\rho D_{vapour}\nabla Y_{vapour}) + R_{vapour} + \dot{m}_{vapour} \tag{9}$$

where Y_{vapour} is the mass fraction of the water vapour, D_{vapour} is the diffusion coefficient for the water vapour, R_{vapour} is the rate of evaporation (kg/m^2/h), and $\dot{m}_{vapour}$ is the mass transfer rate due to evaporation (mol/s). This value depends upon the nozzle, and the nozzle for the investigation was PJ10 due to its ease of implementation. A nozzle diameter of 1 mm was considered for the simulation. The nozzle specifications and spray pattern are portrayed in Figure 2.

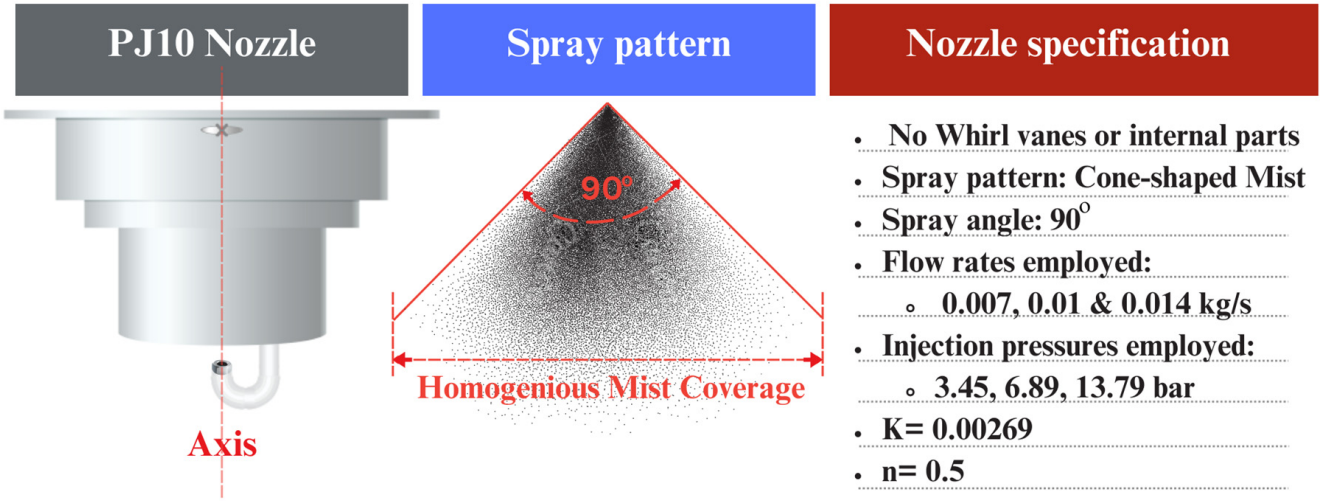

Figure 2. Nozzle specifications and its spray pattern.

The injection pressure in psi was selected according to the datasheet of mist nozzle PJ10. Using the necessary conversion factors, the mass flow rate (m) was calculated in kg/s. The effect of the cooling method and flow rate on the thermal behaviour of the battery cell was analysed, and the values were compared. Using a statistical analysis tool, the most optimum condition was deduced and presented.

The battery's state of health (SOH) was determined at different conditions to adjudicate the most optimised condition of cooling. The SOH calculations were performed using the following equations.

$$\text{SOH} = \frac{Q_{observed}}{Q_{initial}} \times 100 \tag{10}$$

where $Q_{observed}$ is the corresponding observed capacity, Q_{full} corresponds to the capacity obtained from the battery and $Q_{initial}$ is the capacity at the initial case condition.

The battery model was developed in ANSYS Fluent and to determine the SOH, which depends on the peak temperature during the working condition, capacity was defined as a function of temperature.

$$Q(T) = Q_0 \cdot f(T) \tag{11}$$

where $Q(T)$ is the temperature-dependent capacity, $Q_0 \cdot$ is the nominal capacity at the observed temperatures and $f(T)$ denotes the function that describes how capacity changes with temperature. The function considered here was assumed to be exponential, and the relationship was defined, as shown in Equation (12).

$$f(T) = e^{\left(\frac{T - T_{ref}}{k}\right)} \tag{12}$$

where T is the observed temperature, T_{ref} is the reference initial temperature and k is the temperature coefficient. The temperature coefficient was found using Equation (13).

$$k = \frac{\Delta C}{C_o \cdot \Delta T} \tag{13}$$

where ΔC is the change in capacity, C_o is the initial capacity and ΔT is the temperature change.

$$Q_{new} = Q_{initial} \cdot e^{\left(\frac{T_{observed} - T_{initial}}{k}\right)} \tag{14}$$

The equations were substituted to solve and find the Q_{new}

$$(1 - a) * \ln(a) = C \tag{15}$$

$$\text{where } C = \left(T_i - T_0\right)^2 \text{ and } a = \frac{Q_{observed}}{Q_{initial}} \tag{16}$$

Upon solving the equation using the Newton–Raphson method executed through the PYTHON code, the value of Q_{new} was obtained for each case of iteration and, thus, SOH was determined.

3. Results and Discussion

For the numerical simulation, the inlet air velocity (V) and injection pressure (P) were considered as the control parameters. The simulation was carried out under different magnitudes of these control parameters, and the outcomes are presented in Table 2. The maximum cell temperature (T_{max}) is considered the main response from the simulation.

To improve our understanding, the Results and Discussion section is organised in a manner like when the effect of air velocities on the temperature attenuation characteristics of the battery was first elaborated on. This represents stand-alone air cooling and shows the maximum temperature reduction potential. This is followed by the explanation of the effect of injection pressure, which can change the droplet size, cause subsequent evaporation and, thus, facilitate temperature reduction potential. Finally, the effect of the combination

of air velocities and mist injection pressure was envisaged. For all cases, the temperature distribution on and around the cell surface was visualised as contour plots. The results are promising in the scenario of a multi-strategical approach rather than stand-alone air cooling, especially when the battery is put under high discharge rates.

Table 2. Outcomes of the numerical simulation and SOH estimation.

Sl. No	V (m/s)	P (bar)	m (kg/s)	T_{max} (°C)	SOH (%)
0	0	0	0.000	587.32	9.73
1	10	0	0.000	102.23	44.96
2	15	0	0.000	94.14	52.96
3	20	0	0.000	82.14	64.95
4	25	0	0.000	76.20	71.95
5	0	3.5	0.007	118.92	83.72
6	0	7	0.010	97.63	85.91
7	0	14	0.014	82.31	86.70
8	10	3.5	0.007	75.81	89.45
90	10	7	0.010	76.49	89.19
10	10	14	0.014	77.30	89.00
11	15	3.5	0.007	67.64	91.22
12	15	7	0.010	65.38	91.80
13	15	14	0.014	66.41	91.44
14	20	3.5	0.007	64.63	91.72
15	20	7	0.010	63.46	92.35
16	20	14	0.014	61.97	92.72
17	25	3.5	0.007	58.74	93.66
18	25	7	0.010	57.02	94.15
19	25	14	0.014	58.29	93.87

3.1. Impact of Air Velocities on Temperature Attenuation

The simulation was carried out in the absence of mist and with different air velocities (0, 10, 15, 20 and 25 m/s) over a 21,700 lithium-ion battery at a 4C discharge rating. The different levels of air velocities were selected based on the realistic driving conditions of an electric two-wheeler. The effect of air velocities in reducing the cell's peak temperature is presented in Figure 3. With increasing air velocities, the peak cell temperature was found to decrease. The obtained trend was aligned with the results of previous researchers [22–25]. Despite the results being positive, it is evident that even at a maximum air velocity of 25 m/s, the attained peak cell temperature was 76.2 °C. Exposing a lithium-ion battery cell to temperatures above 80 °C would always be harmful, which pushes for accelerated cell degradation. This could eventually reduce the longevity and capacity of the battery cell. At an air velocity of 10 m/s, the peak cell temperature was determined to be 102.3 °C. This corresponds to the battery's SOH of about 45% and is also dangerously near the threshold of a chain reaction leading to thermal runaway. The observed peak temperature of 76.2 °C at 25 m/s may reduce the chances of thermal runaway, but still, this corresponds to an SOH of about 72%. The simulation trials performed with different air velocities disclosed that forced air cooling was not sufficient to keep maximum cell temperature within safe limits, especially when the battery is operated at the discharge rating of 4C or higher.

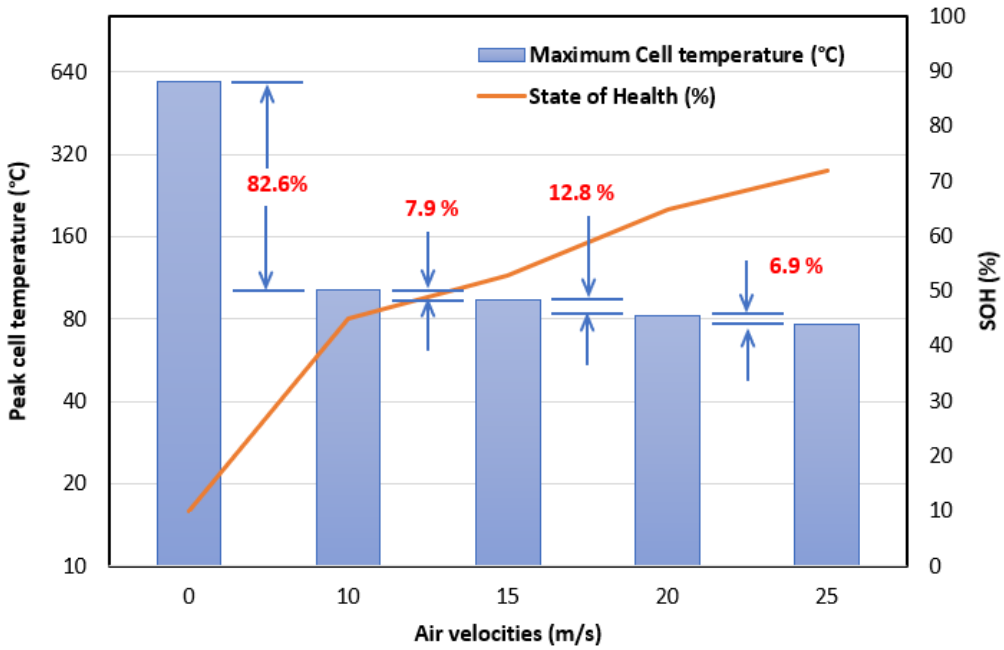

Figure 3. Impact of air velocities on maximum cell temperature and SOH.

The reduced peak cell temperature helps in improving the SOH of the battery, as the capacity is the function of temperature. When the air velocity is increased to 10 m/s from the no cooling condition, the maximum cell temperature is reduced by 82.6%. But when it is increased from 20 m/s to 25 m/s, the % reduction in cell temperature is only about 6.9%. It can be interpreted that an increase in air velocity beyond a certain limit does not cause a drastic drop in the maximum cell temperature and helps temperature attenuation.

3.2. Impact of Injection Pressure on Temperature Attenuation

The thermal attenuation characteristics of mist cooling are analysed by simulating the water mist produced through a PJ10 nozzle with injection pressures of 3.5, 7 and 14 bar in the sequence with zero inlet air velocity in all cases. The simulation results evidenced that mist cooling aids in thermal attenuation were less effective than forced convection by about 5 to 8%. The attained results matched with previously reported research works [26–29]. Since the injection pressure considered was on the higher end of the pressure spectrum, the injection moved in with a larger inlet velocity, creating a jet of fluid that followed a straight path downwards and escaped the control volume with minimal contact with the surface area of the cell. The absence of sufficient turbulence, which could aid in distributing the cooling through an increased percentage of contact, aiding the vaporisation of fluid for inducing temperature attenuation effect over the surface area of the cell, restricted the mist cooling strategy from exerting its utmost effectiveness, hence causing the comparative increase in peak temperature.

Figure 4 represents the variation in peak cell temperature and the corresponding SOH at different injection pressures. The percentage of deviation from zero to 3.5 bar was 79.8%, which is a substantial amount, inferring the magnitude of positive thermal attenuation. As the injected pressure increased from 3.5 to 7 and then again to 14 bar, the percentage of depreciation in the temperature reduction also reduced from 17.9% to 15.7%, indicating that increasing injection pressure beyond 14 bar does not serve to increase temperature attenuation. The lowest peak cell temperature observed was 82.31 °C, which is higher compared to forced convection. It also indicates that the mist cooling strategy is not sufficient to act effectively as a stand-alone cooling system at higher C-rated conditions.

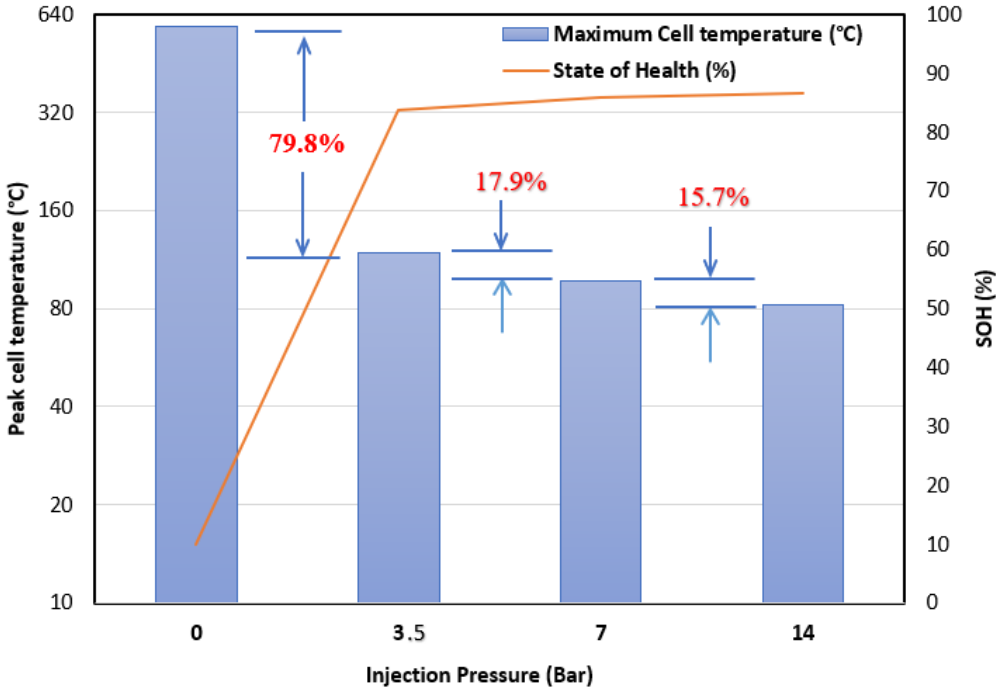

Figure 4. Impact of mist cooling injection pressure on maximum cell temperature and SOH.

3.3. Combinational Influence of Forced Convection and Mist Cooling

It is essential to investigate the combined influence of forced convection velocities and mist injection pressures on the thermal attenuation characteristics as in the case of multi-strategical approaches. It can be inferred from the results that the maximum attenuation of the cell temperature happens at the injection pressure of 7 bar and air velocity of 25 m/s. The contour plot of cell temperature at the specified condition is presented in Figure 5. Due to the forced convection, there is a positive chamfer in the angle of the spray, which, in turn, increases the spread and effectiveness of the mist application. The area where the mist is introduced could be correlated with its effectiveness and, thus, temperature attenuation.

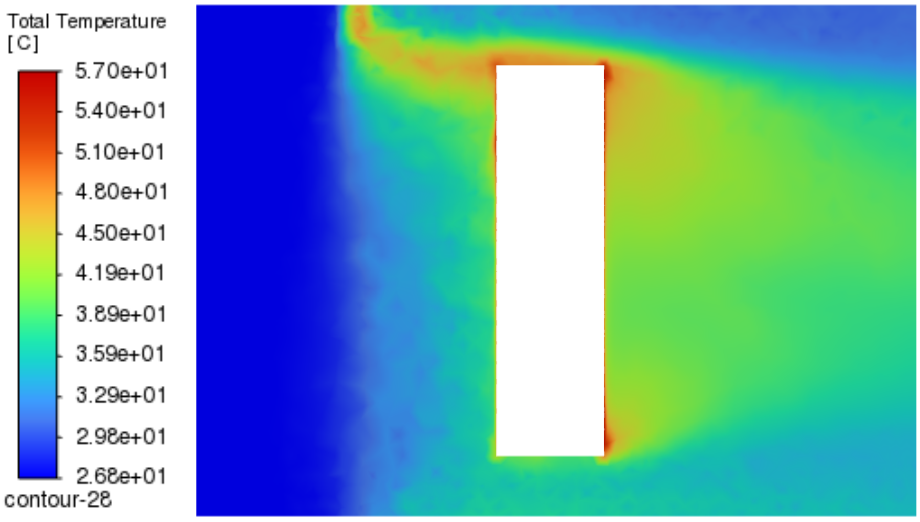

Figure 5. Contour plot of temperature for the battery cell (V = 25 m/s, P = 7 bar).

Figure 6 disclosed that at the increase in air velocity for each injection pressure, the peak cell temperature decreased. The rate of decrease can be understood by the slope connecting the three points of the bar chart. It can be concluded that the maximum effect of depreciation occurs at 20 m/s and, thereafter, the rate of depreciation is lower. Hence, it is

concluded that at a high C-rating (like 4C in the present study), 20 m/s offers a maximum change in peak temperature as the injection pressure is increased. Further investigation of results showed that the total area of exposure from the mist is a function of air velocity and injection pressure. The combination of these variables opens a unique regime of results. Here, the product of air velocity and injection pressure dictates the overall surface area of the cell that is exposed to the mist, i.e., if the air velocity is higher in comparison to the injection pressure, the dominant factor is air velocity, and the mist injection is overpowered which, in turn, creates a condition where a major part of mist is only exposed to the upper part of the battery. This results in the lower effectiveness of the mist injection condition and, hence, lower attenuation of peak temperature. The spread is still present, but most of the mist is carried away by the forced convection. The contour plot for the case of air velocity at 25 m/s and the injection pressure of 4 bar is presented in Figure 7.

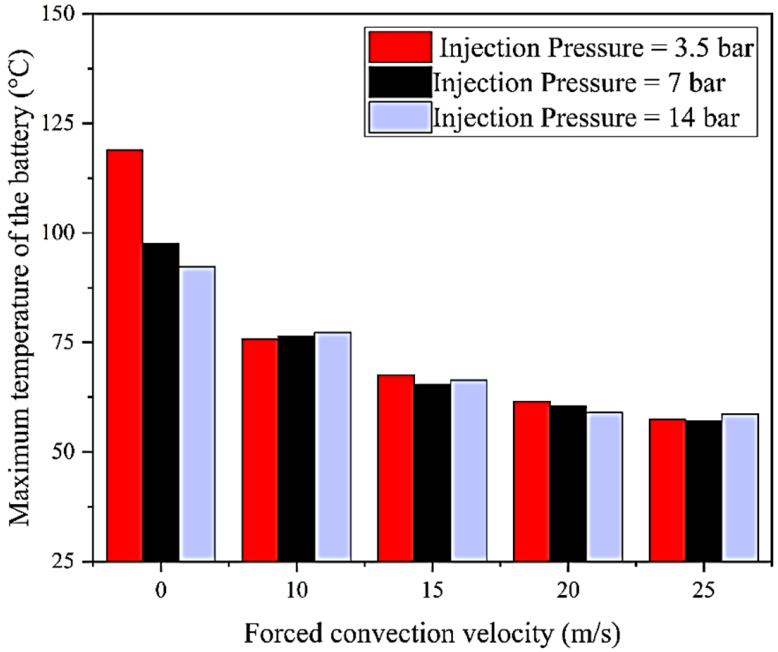

Figure 6. Influence of forced air velocity over peak temperature.

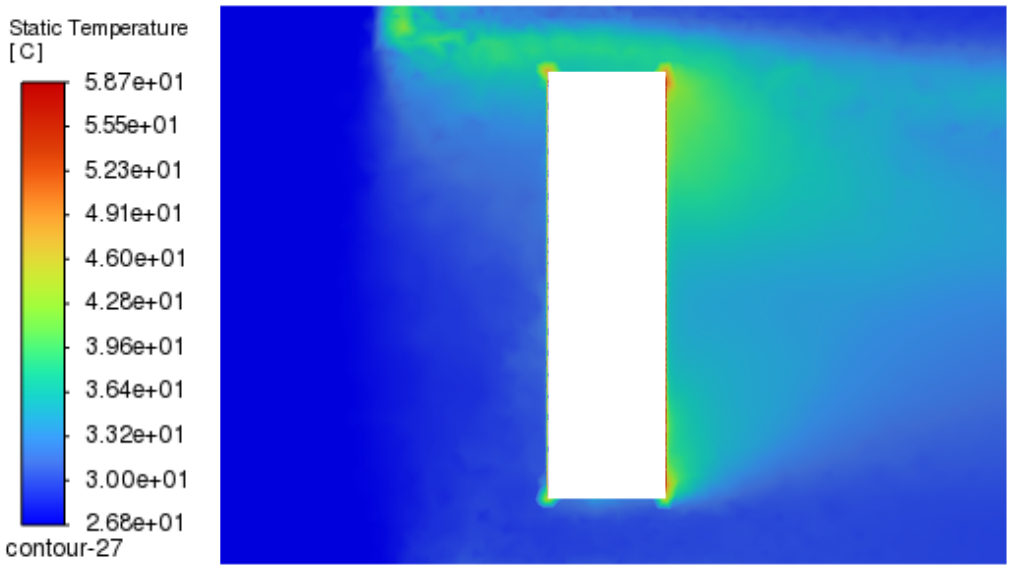

Figure 7. Reduced influence of mist injection at the bottom surface cell due to larger air velocity.

Whilst the injection pressure is predominant over air velocity, the maximum area over which the mist is exposed is the bottom part of the cell. A velocity magnitude contour over the central XY plane is created to showcase the effect of injection pressure overwhelming the effect of forced air convection. This is shown in Figure 8. This condition also corresponds to lower effectiveness and, hence, lower temperature attenuation. This is evidenced in the case of air velocity at 15 m/s and an injection pressure of 14 bar. This is shown in Figure 9. Similar to this is the case when the air velocity overwhelms the injection pressure, the only difference being that the velocity follows a trajectory over the upper part of the battery.

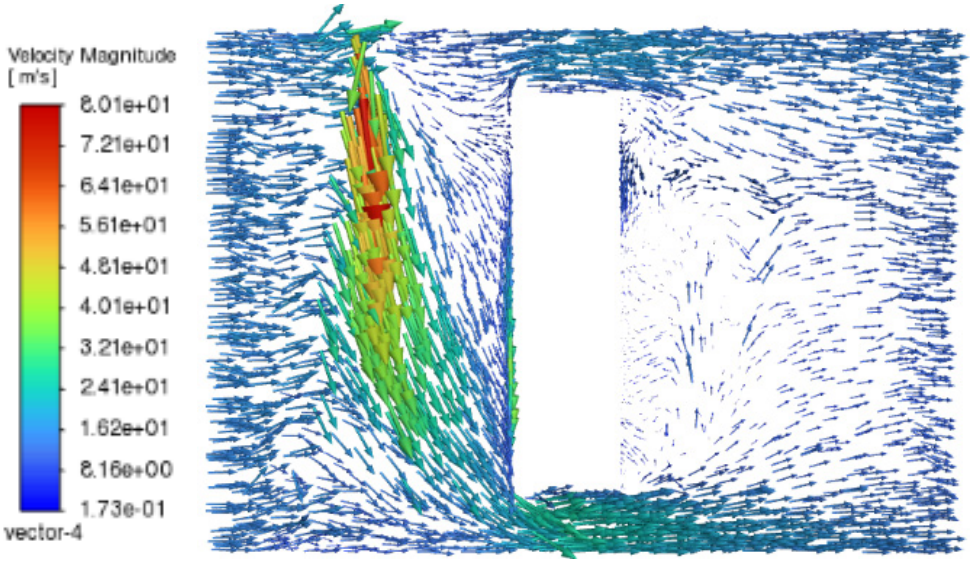

Figure 8. Flow pattern where injection pressure overwhelms air inlet velocity.

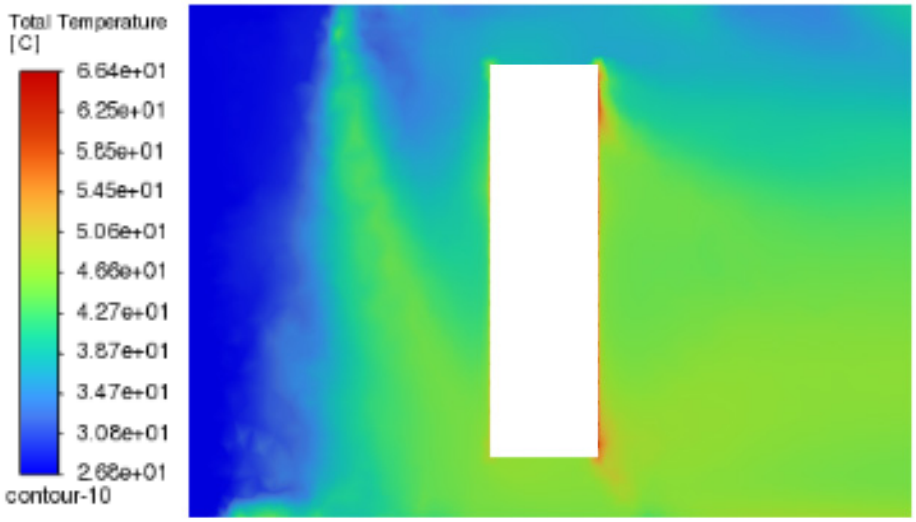

Figure 9. Temperature contour at a high injection pressure of 14 bar.

The influence of injection pressure change is graphically shown in Figure 10. The trend indicates that as the injection pressure increases for each escalating value of inlet air velocity, the peak temperature is reduced, which implies that an increase in injection pressure positively affects the temperature management of the battery. Upon closer inspection, the correlational plot is created, and from the graph, the variations in the case of each strategy are identified as independent as well as multi-strategical. It is suggested that the multi-strategical approach provides better temperature attenuation and SOH over a single strategical approach.

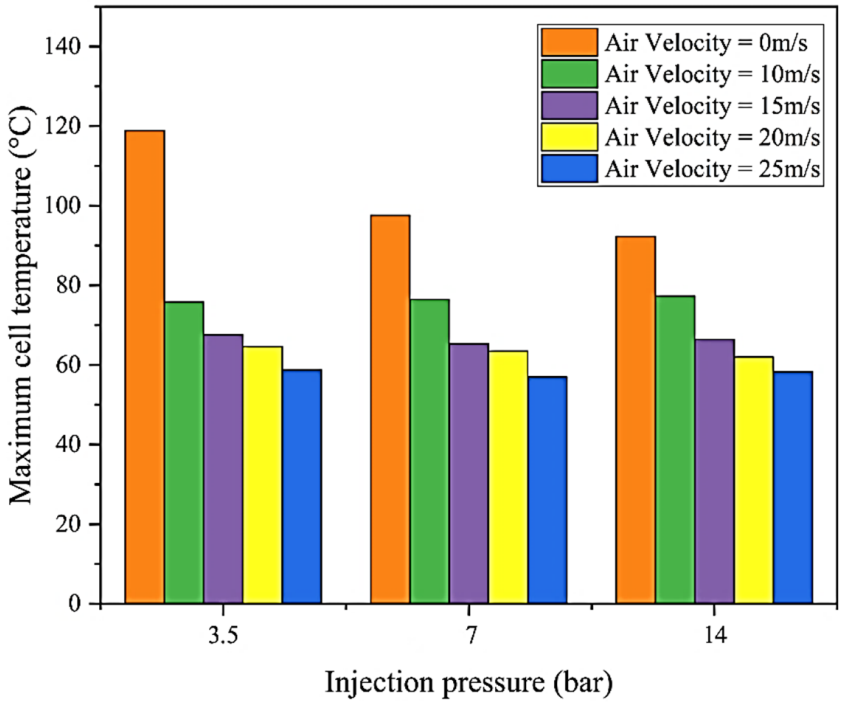

Figure 10. Influence of injection pressure over different air velocities.

3.4. Interpretation of SOH in Different Strategies

The interpretation of SOH for the battery cell is performed over the entire spectrum of cases considered in the present study. The notation is as follows: (a) case 0—no cooling, (b) cases 1 to 4—standalone forced air cooling system, (c) cases 5 to 7—standalone mist cooling, and (d) cases 8 to 19—a multi-strategical cooling approach that combines the forced air and mist cooling. This is shown in Figure 11.

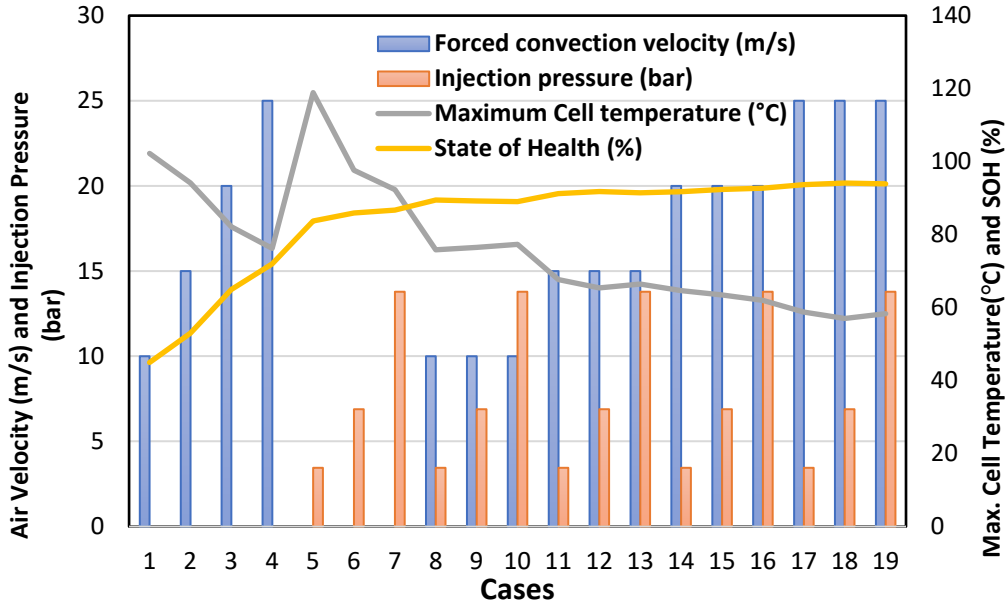

Figure 11. Correlational chat of cell peak temperature and SOH.

Under 4C conditions, the cell's peak temperature can reach up to 587.32 °C, which causes thermal runaway, indicating the absolute essentiality of a cooling system. The corresponding SOH is merely 9.7%. In a forced air-cooling system, despite the employment of higher velocities, it is not enough to maintain the cell temperature out of the thermal

runaway danger region. It is also clear that a system with mist cooling alone is not so effective at accomplishing the above task. The combinational approach proves itself to be more effective as it can reduce the peak temperature to 57.02 °C. The simulated conditions reveal the requirement of a balance between air velocity and injection pressure for increased effectiveness, as explained in the previous session. The corresponding growth in SOH can be seen in the graph, indicating the positive impact of the multi-strategical approach, reaching up to 94.15%.

3.5. Integration of Airflow Improviser

To tackle the anomalies occurring with the variation in airflow velocities and injection pressures, an airflow improviser (AFI) is introduced into the system. The literature revealed that the addition of an airflow improviser provides a promising strategic reconciliation of variables. Hence, AFI was added to the control volume to induce increased turbulence and control the channelling of inlet airflow. This is an alternative approach for balancing variables. The control volume with AFI is shown in Figure 12.

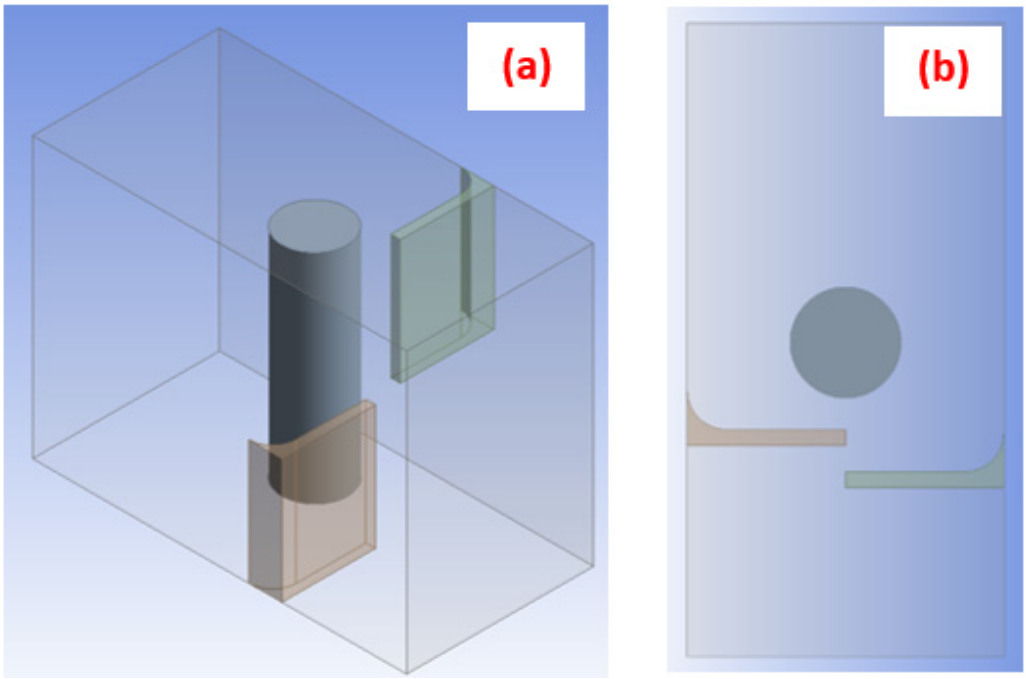

Figure 12. Reconstructed control volume with AFI (**a**) isometric view and (**b**) top view.

There are two plane sheets attached to the edges of the top wall and the bottom wall, with the edges coinciding with the control volume wall showing a fillet radius of 7.5 mm, constituting 25% of the total length of AFI at 30 mm. The top AFI is placed 85 mm from the inlet, and the bottom AFI is placed 77 mm from the inlet. The strategic placement of AFIs is performed to ensure the balancing of variables. The first kind of discrepancy in peak cell temperature is experienced when the airflow velocity is greater than the injection pressure. Under this situation, the top AFI helps to re-channel the flow towards the cell surface. Since considered air velocities are in a higher considerable range, the AFI is placed 24 mm away from the centre of the cell to induce a reverse flow without causing too much disturbance in the cell temperature domain. The second condition is where the injection pressure overwhelms the airflow velocity, and the injection of the fluid falls mostly towards the bottom of the control volume. For this reason, the bottom AFI is placed comparatively near the top AFI so that the flow is reversed and combines with air flow velocity, thus aiding in peak cell temperature attenuation. The inclusion of AFI creates increased turbulence inside the control volume. Figure 13b represents the path lines of flow particles, while Figure 13c shows the flow pattern change and the effect of the increased turbulence over

cell peak temperature. The effect of airflow improviser on temperature reduction and SOH enhancement is presented in Table 3.

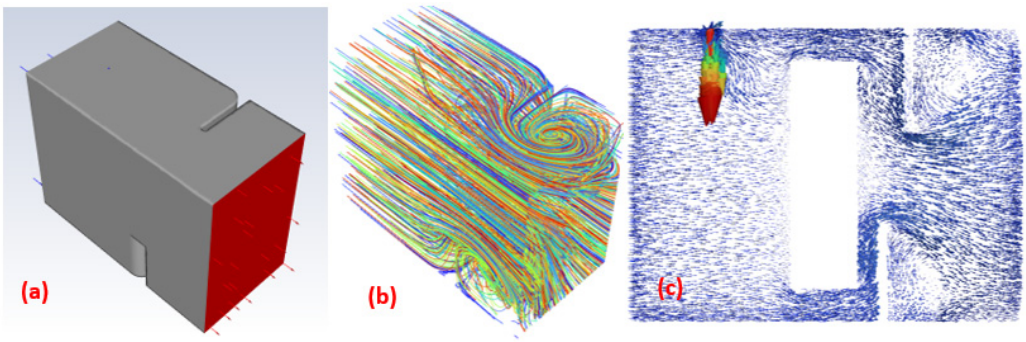

Figure 13. (**a**) Re-designed control volume with AFI. (**b**) Flow path lines of particles showing increased turbulence and (**c**) velocity contour after 1 s.

Table 3. Effect of airflow improviser on temperature reduction and SOH enhancement.

Sl. No	V (m/s)	P (bar)	Peak Cell Temperature (°C)		% Reduction in Temp.	SOH (%)		% Improvement in SOH
			Without AFI	With AFI		Without AFI	With AFI	
20	10	14	77.30	74.81	3.22	89.00	91.74	3.07
21	15	7	65.38	63.94	2.20	91.80	93.45	1.79
22	20	7	63.46	61.22	3.53	92.35	93.94	1.72
23	25	3.5	58.74	56.39	4.00	93.66	94.78	1.19
24	25	7	57.02	54.73	4.02	94.15	95.15	1.06

The new control volume is represented in Figure 13a. The red colour indicates the outlet. The AFI creates disruptions in the path of airflow and fluid mist flow. This discrepancy is channelled towards the hotspots of the battery peak cell temperature, which, in turn, alleviates the cell peak temperature due to the greater surface area of the cell being exposed to the cooling effect and with better turbulence intensity.

The temperature contours showcased in Figure 14a–d exhibit the positive impact of AFI on thermal attenuation. All these results demonstrate that a further reduction in peak cell temperature is possible by employing AFI. This is also manifested from the simulation results shown in Figure 14e. Even for the best scenario, the peak cell temperature could be reduced with the incorporation of AFI. The impact of AFI on the cell peak temperature over a range of air velocities and injection pressures is portrayed in Figure 15.

There is about a 4.2% reduction in peak cell temperature at an air velocity of 25 m/s and injection pressure of 7 bar; to conclude, an average of about a 4.2% reduction in peak temperature is achieved by the application of an AFI. The conundrum that induces further improvisation over the system is the prevalence of comparatively higher cell peak temperatures. This is appropriated by the application of additives at a specific concentration to water to further enhance the heat transfer capability of the working fluid.

Figure 16 indicates that AFI has a positive impact on attenuating the cell peak temperature. The improvement in SOH, as well as peak cell temperature attenuation, is illustrated. Despite the improvement in SOH, a declining trend is observed in %. It was 2.98% in the initial stage, which dropped to 1.06% in the final stage. On the contrary, the rate of reduction in peak cell temperature increased from 3.22% to 4.02% after each considered case.

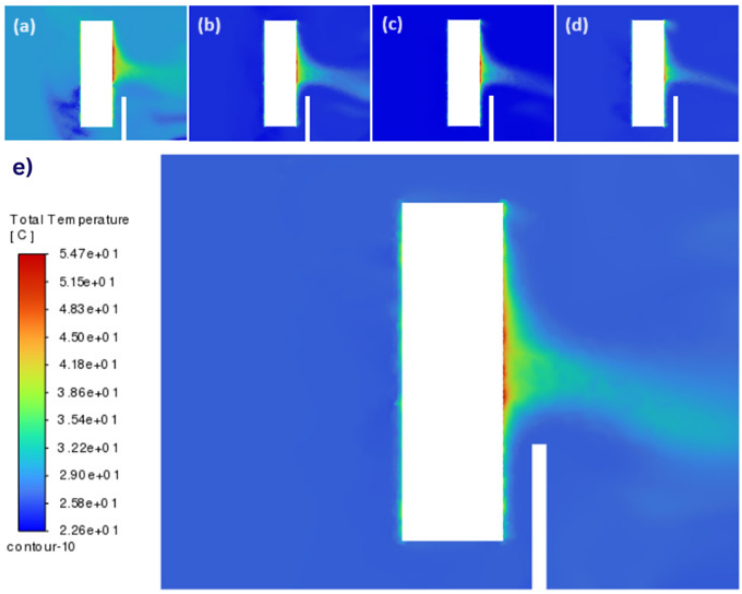

Figure 14. Simulated temperature contours in a combinational approach when (**a**) V = 15 m/s, P = 7 bar, (**b**) V = 20 m/s, P = 7 bar, (**c**) V = 25 m/s; P = 3.5 bar, (**d**) V = 25 m/s; P = 7 bar, and (**e**) V = 25 m/s; P = 7 bar with AFI.

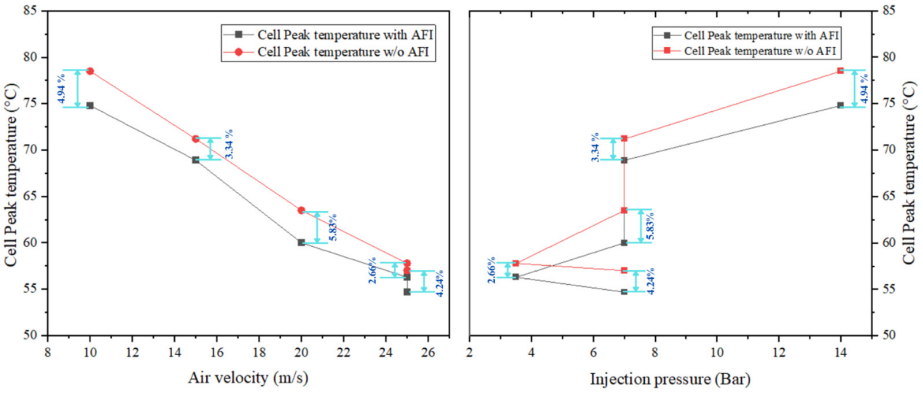

Figure 15. Impact of AFI on the cell peak temperature over a range of air velocities and injection pressures.

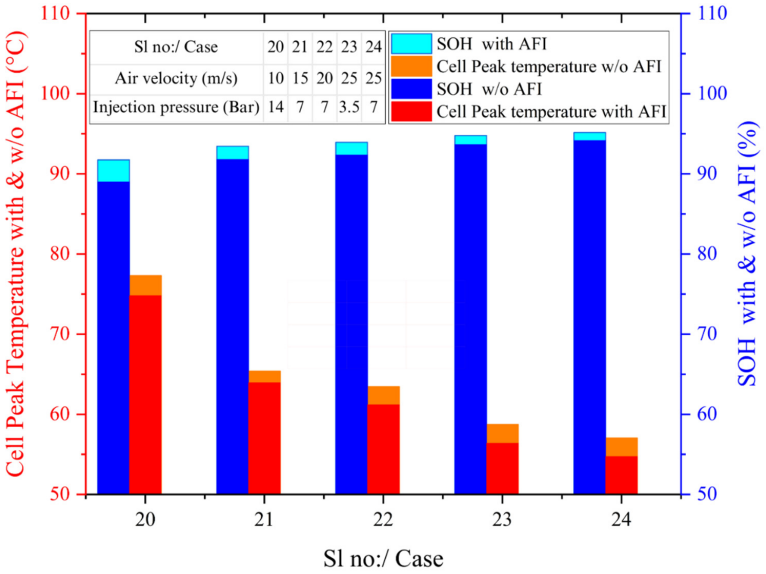

Figure 16. Cell peak temperature and SOH variations due to AFI.

3.6. Impact of Additive Inclusion on Thermal Attenuation Characteristics

Until this point, the working fluid used for mist cooling was water. This was exercised due to its ease of availability and cost-effectiveness. But to retaliate the thermal runaway (TR) under higher C-rate conditions, certain additives could be mixed with water. Several studies were conducted to identify the best fluids and their mixing concentrations [30–36] with a compromise on thermal attenuation properties. Porous materials like nickel foam, glass wool and nanoporous aerogel, due to their internal pore diameter characteristics and range of lower heat conduction and higher temperature resistance, despite being a good contender in TR rectification, are not suitable for the particularity of this problem. In another study, N_2-Twin-liquid $C_6F_{12}O$ mist was used. The thermal attenuating property was overwhelmed by the production of harmful byproduct gases and was not recommended [37]. Another study compared $C_6F_{12}O$ with CO_2 and HFC227ea, which were used as gas constituents along with water mist for TR regulation [38]. The observed effect was positive but was not capable enough to keep the thermal conditions under check in real time. The literature review disclosed that properties like droplet size, contact angle, thermal conductivity, particle arrangement in the chemical substrate, surface tension, foamability, foaming volume, reaction properties, etc., play crucial roles in the thermal attenuation characteristics. From the previous studies, it was found that additives with lower surface tension and foamability possess enhanced cooling effectiveness and, hence, from the data acquired from the research papers, Tween 20, Tween 80, 1-heptanol, FS3100 and APG0810 were selected as additives. Also, to address the foamability issue, a deformer (0.1%) was added to each combination with water to enhance the bubble rupture, which, in turn, coiled for a comprehensive and comparative study, except 1-heptanol since it is an anti-foaming agent. The addition of more than one additive or combination of additives does not serve further thermal attenuation, and hence, a single additive with a 3% concentration was selected, according to the literature. ANSYS simulation using the volume of fluid for discrete phase modelling was executed, and necessary variable and property values were imported through the above calculations extracted from reference studies. The simulations were conducted at the best case acquired from the previous simulations, and the results were tabulated. The properties of the selected additives are shown in Table 4, along with the simulation output results. From Table 4, it is evident that under a higher C rating ($\leq$4), the multi-strategical cooling approach involving forced convection, water mist cooling, which is further coupled with AFI, and additives could deliver the maximum thermal attenuation conditions to keep the battery under thermally stable condition.

Table 4. Temperature and SOH calculations for the system with AFI and different additives.

Sl. No	Additive Name	Type	Chemical Formula	Surface Tension (mN/m)	Contact Angle (°)	Peak Cell Temp. (°C)	% Reduction in Temp.	SOH (%)
25	1-heptanol	Alcohol	$C_7H_{15}OH$	50.6	20.0	48.24	11.86	96.02
26	FS3100	Non-ionic surfactant	$C_{20}H_{28}F_{13}O_7$	33.52	46.6	50.21	8.26	95.48
27	Tween 20	Non-ionic surfactant	$C_{18}H_{34}O_6$ $(C_2H_{4O})_{20}$	28.6	71.2	49.54	9.48	95.62
28	Tween 80	Non-ionic surfactant	$C_{24}H_{44}O_6$	42.1	67.9	47.43	13.34	96.13
29	APG0810	Non-ionic surfactant	$C_{16}H_{32}O_6$	27.64	34.6	48.94	10.58	95.71

The impact of the additive addition on thermal attenuation characteristics is exhibited in Figure 17a,b. For this specific investigation, the best case in the form of a combinational cooling approach was considered. Water mixed with 3% (by wt.) of tween 80 additives can reduce the peak temperature by about 13.34%. Among the additives, minimal performance is observed with FS 3100, but still, the peak temperature can be lowered by 8.26% compared

to unadulterated water. The pathline contour obtained for these two cases is, respectively, shown in Figure 17c,d. Greater turbulence and the formation of smaller eddies were observed with Tween 80. This helped enhance the turbulence intensity in the flow field, thereby increasing the heat transfer between the battery surface and the working fluid. Figure 17 showcases both the best-case temperature depreciation due to the addition of Tween 80, constituting about a 13.34% reduction, as well as the highest peak cell temperature observed with FS3100, which still managed to reduce the peak temperature by 8.26%. This indicates that the addition of additives with water, along with the corresponding deformer, could positively contribute to a reduction in cell peak temperature. The differences in path lines plotted from the particle ID showcase the movement of particles inside the control volume. In comparison, Figure 17c shows much more turbulence and the formation of smaller eddies, which enhanced the turbulence intensity in the flow, thereby increasing the heat transfer between the increased accessible surface of the battery and the working fluid. The positive influence of additives on temperature attenuation and SOH enhancement is illustrated in Figure 18. Through the simulation, the effectiveness of additives was evaluated. It followed the order Tween 80 > 1-Heptanol > APG0810 > Tween 20 > FS3100. The lowest peak temperature was noticed with the airflow improviser at the air velocity of 25 m/s and injection pressure of 7 bar with the working fluid of water adulterated with Tween 80.

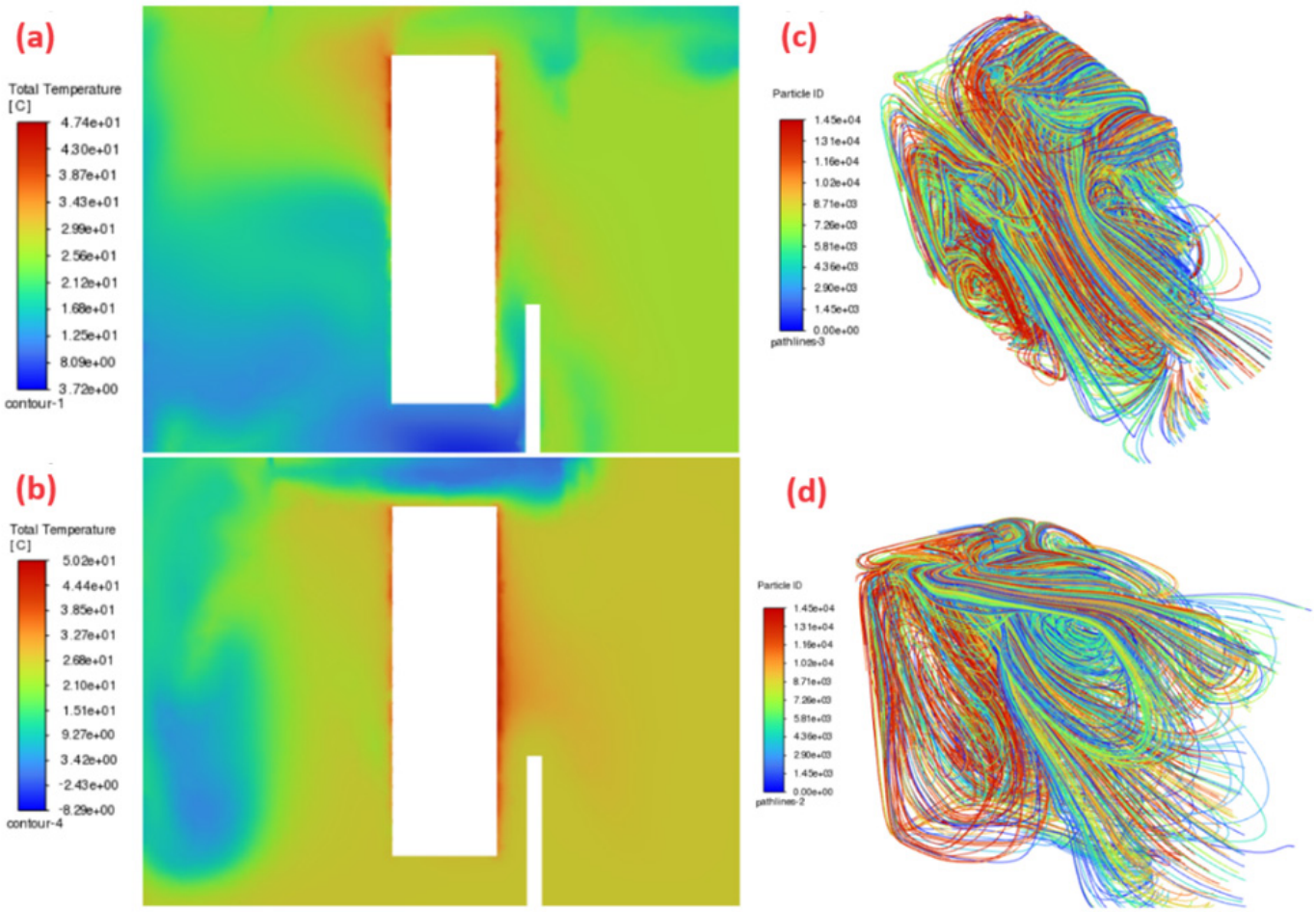

Figure 17. Impact of additive addition on cell temperature for (**a**) the case of maximum reduction and (**b**) the case of minimum reduction (**c**,**d**) with the path line contour showing the increased turbulence distribution.

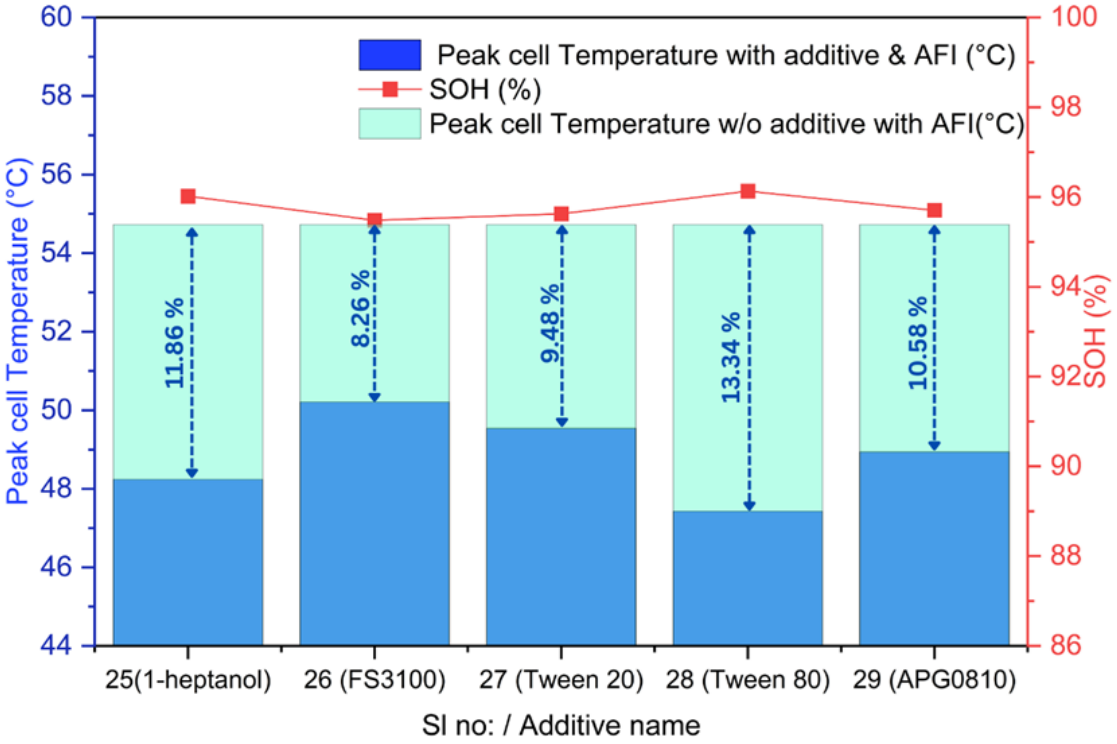

Figure 18. Influence of additive type on peak cell temperature and SOH.

The addition of the Tween 80 additive showcased the best temperature attenuation and controlled the peak temperature at 47.43 °C, which is the well-suited temperature for the optimal working of the battery. Hence, we can conclude that the combination approach of forced convection and mist cooling, along with the employment of AFI and the addition of additives, creates a solution capable of controlling the battery peak temperature under optimal working conditions.

4. Conclusions

In the present study, the thermal attenuation characteristics of a combinational cooling approach involving forced convection and mist cooling were numerically investigated, especially under the 4C rating. Different magnitudes replicating the real running conditions of an electric two-wheeler were considered for air velocities and injection pressures. The impact of introducing an air flow improviser and compositional changes in the working fluid through additives were also exhaustively examined. The major concluding remarks are presented below:

Under the 4C rating, the adoption of a single cooling scheme, such as forced air cooling or mist cooling, was discovered to be ineffective and demonstrated the need for combinational cooling strategies.

In the combinational cooling strategy, the maximum temperature attenuation was achieved at the air velocity of 25 m/s and injection pressure of 7 bar. This is 25.17% higher than the standalone forced air cooling and 30.72% higher than the standalone mist cooling approaches. The estimated SOH of the battery is also at a maximum (~94%) in this condition. When the injection pressure is increased beyond 7 bar, it is observed that the interference occurs between mist cooling and forced air cooling, which ultimately results in less temperature attenuation and a compromise on SOH.

The simulation results affirm the positive impact of the inclusion of an airflow improviser on temperature attenuation and tackling the anomalies which disrupt the temperature attenuation due to the overwhelming influence of one control parameter over another (i.e., air velocity and injection pressure). Even under the best-case scenario, the cell peak temperature is further reduced by about 4.02% with the inclusion of an airflow improviser.

SOH follows a pattern of incremental increase in the % over the increase in air velocity and injection pressure. The average percentage of the SOH increase was 1.74% among all cases, whereas the max and min were 2.98% and 1.06%, respectively.

The compositional changes in working fluid through additives evidence that thermal attenuation is advantageous with all additive types (with the descending order of effectiveness for the additive being Tween 80 > 1-Heptanol > APG0810 > Tween 20 > FS3100) considered in the present investigation. However, the effectiveness varied among the additives and tween 80 surpassed all other additives in thermal attenuation and SOH enhancement characteristics. An average of about an 11% reduction in maximum cell temperature was observed with the additives, with its best case (Tween 80) amounting to 13.34%. The corresponding estimated SOH had a maximum of 96.13%.

The present study exposes the supremacy of multi-strategical (combinational) approaches in thermal attenuation characteristics over single-strategical approaches. Also, promising results were obtained with the inclusion of airflow improvisers and additives in the working fluid. Future research works can be oriented towards exploring the adoption of different working fluids, different concentrations for the additives and the implementation of a twirling nozzle injection on the effectiveness of the cooling system. The anomalies that occurred due to the overwhelming air velocity in forced convection or injection pressure in the mist injection highlight the necessity of a balance ratio coefficient, which could also be explored in future studies.

Author Contributions: Conceptualization, K.C. and A.M.; methodology, K.C.; software, A.M.; validation, A.M.; formal analysis, A.M.; investigation, A.M.; resources, K.C.; data curation, K.C.; writing—original draft preparation, A.M.; writing—review and editing, K.C.; visualization, A.M.; supervision, K.C.; project administration, K.C.; funding acquisition, K.C. All authors have read and agreed to the published version of the manuscript.

Funding: This research received no external funding.

Data Availability Statement: The original contributions presented in the study are included in the article, further inquiries can be directed to the corresponding author.

Conflicts of Interest: The authors declare no conflict of interest.

References

1. Konovalov, D.; Tolstorebrov, I.; Eikevik, T.M.; Kobalava, H.; Radchenko, M.; Hafner, A.; Radchenko, A. Recent Developments in Cooling Systems and Cooling Management for Electric Motors. *Energies* **2023**, *16*, 7006. [CrossRef]
2. Maiorino, A.; Cilenti, C.; Petruzziello, F.; Aprea, C. A Review on Thermal Management of Battery Packs for Electric Vehicles. *Appl. Therm. Eng.* **2024**, *238*, 122035. [CrossRef]
3. Wang, Y.; Biswas, A.; Rodriguez, R.; Keshavarz-Motamed, Z.; Emadi, A. Hybrid Electric Vehicle Specific Engines: State-of-the-Art Review. *Energy Rep.* **2022**, *8*, 832–851. [CrossRef]
4. Haghani, M.; Sprei, F.; Kazemzadeh, K.; Shahhoseini, Z.; Aghaei, J. Trends in Electric Vehicles Research. *Transp. Res. D Transp. Environ.* **2023**, *123*, 103881. [CrossRef]
5. Kannan, C.; Vignesh, R.; Karthick, C.; Ashok, B. Critical Review towards Thermal Management Systems of Lithium-Ion Batteries in Electric Vehicle with Its Electronic Control Unit and Assessment Tools. *Proc. Inst. Mech. Eng. Part D J. Automob. Eng.* **2021**, *235*, 1783–1807. [CrossRef]
6. M, A.; C, K. Mitigation of Thermal Runaway in Air Cooled Li-Ion Batteries Using a Novel Cell Arrangement Coupled with Air Flow Improviser: A Numerical Investigation and Optimization. *Numer. Heat Transf. Part B Fundam.* **2023**, *85*, 736–756. [CrossRef]
7. Akinlabi, A.A.H.; Solyali, D. Configuration, Design, and Optimization of Air-Cooled Battery Thermal Management System for Electric Vehicles: A Review. *Renew. Sustain. Energy Rev.* **2020**, *125*, 109815. [CrossRef]
8. Heidarshenas, B.; Sina, N.; El-Shafay, A.S.; Saleem, S.; Sharifpur, M. The Effect of the Zigzag Arrangement of Lithium-Ion Batteries inside the Air Duct of an Office Building for Heating and Evaluation of the Impact of the Number of Air Outlets in Different Seasons of the Year. *J. Energy Storage* **2022**, *50*, 104204. [CrossRef]
9. Saw, L.H.; King, Y.J.; Yew, M.C.; Ching Ng, T.; Chong, W.T.; Pambudi, N.A. Feasibility Study of Mist Cooling for Lithium-Ion Battery. *Energy Procedia* **2017**, *142*, 2592–2597. [CrossRef]
10. Zhu, Y.; Zhou, Y.; Gao, H.; Wang, Z.; Bai, W.; Ouyang, D.; Wang, J. Synergistic Inhibition of Thermal Runaway Propagation of Lithium-Ion Batteries by Porous Materials and Water Mist. *J. Clean. Prod.* **2023**, *406*, 137099. [CrossRef]
11. Zhang, Y.; Peng, W.; Liu, X.; Ren, J.; Zang, X.; Xie, Q.; Li, J. Experimental Study on Suppression of Thermal Runaway in Lithium-Ion Battery by Mixed Particle Size Water Mist. *Process Saf. Environ. Prot.* **2023**, *179*, 189–198. [CrossRef]

12. Liu, T.; Huang, J.; Hu, X.; Hu, J.; Wang, X. Experimental Study on the Cooling Effect of Fine Water Mist on the Thermal Runaway in a Single Lithium Ion Battery. *Appl. Therm. Eng.* **2024**, *240*, 122194. [CrossRef]
13. Xu, J.; Duan, Q.; Zhang, L.; Liu, Y.; Zhao, C.; Wang, Q. Experimental Study of the Cooling Effect of Water Mist on 18650 Lithium-Ion Battery at Different Initial Temperatures. *Process Saf. Environ. Prot.* **2022**, *157*, 156–166. [CrossRef]
14. Al Hallaj, S.; Maleki, H.; Hong, J.S.; Selman, J.R. Thermal Modeling and Design Considerations of Lithium-Ion Batteries. *J. Power Sources* **1999**, *83*, 1–8. [CrossRef]
15. Liebig, G.; Kirstein, U.; Geißendörfer, S.; Omio, Z.; Schuldt, F.; Agert, C. The Impact of Environmental Factors on the Thermal Characteristic of a Lithium–Ion Battery. *Batteries* **2020**, *6*, 3. [CrossRef]
16. Lisbona, D.; Snee, T. A Review of Hazards Associated with Primary Lithium and Lithium-Ion Batteries. *Process Saf. Environ. Prot.* **2011**, *89*, 434–442. [CrossRef]
17. Čulík, K.; Štefancová, V.; Hrudkay, K.; Morgoš, J. Interior Heating and Its Influence on Electric Bus Consumption. *Energies* **2021**, *14*, 8346. [CrossRef]
18. Małek, A.; Taccani, R. Innovative approach to electric vehicle diagnostics. *Arch. Automot. Eng.* **2021**, *92*, 49–67. [CrossRef]
19. Peng, X.; Ma, C.; Garg, A.; Bao, N.; Liao, X. Thermal Performance Investigation of an Air-Cooled Lithium-Ion Battery Pack Considering the Inconsistency of Battery Cells. *Appl. Therm. Eng.* **2019**, *153*, 596–603. [CrossRef]
20. Chen, K.; Wang, S.; Song, M.; Chen, L. Configuration Optimization of Battery Pack in Parallel Air-Cooled Battery Thermal Management System Using an Optimization Strategy. *Appl. Therm. Eng.* **2017**, *123*, 177–186. [CrossRef]
21. BETE Spray Nozzles, Fabrications, and Engineered Systems Catalog. Available online: https://www.spray-nozzle.co.uk/resource-links/catalogue-group/catalogue-by-nozzle-design (accessed on 1 May 2024).
22. Jiang, Z.; Li, H.; Sun, Z.; Qu, Z. Experimental Study on 18650 Lithium-Ion Battery-Pack Cooling System Composed of Heat Pipe and Reciprocating Air Flow with Water Mist. *Int. J. Heat Mass. Transf.* **2024**, *222*, 125171. [CrossRef]
23. Xu, Z.; Yu, G.; Zhang, T.; Wang, R. Cooling Performance of Battery Pack as Affected by Inlet Position and Inlet Air Velocity in Electric Vehicle. *Case Stud. Therm. Eng.* **2022**, *39*, 102382. [CrossRef]
24. Xu, X.M.; Sun, X.D.; Hu, D.H.; Li, R.Z.; Tang, W. Research on Heat Dissipation Performance and Flow Characteristics of Air-Cooled Battery Pack. *Int. J. Energy Res.* **2018**, *42*, 3658–3671. [CrossRef]
25. Dai, H.; Wang, Y. Study on the Influence of Air Inlet and Outlet on the Heat Dissipation Performance of Lithium Battery. *World Electr. Veh. J.* **2023**, *14*, 113. [CrossRef]
26. Wu, T.; Wang, C.; Hu, Y.; Fan, X.; Fan, C. Research on Spray Cooling Performance Based on Battery Thermal Management. *Int. J. Energy Res.* **2022**, *46*, 8977–8988. [CrossRef]
27. Fan, Y.; Bao, Y.; Ling, C.; Chu, Y.; Tan, X.; Yang, S. Experimental Study on the Thermal Management Performance of Air Cooling for High Energy Density Cylindrical Lithium-Ion Batteries. *Appl. Therm. Eng.* **2019**, *155*, 96–109. [CrossRef]
28. Bao, Y.; Fan, Y.; Chu, Y.; Ling, C.; Tan, X.; Yang, S. Experimental and Numerical Study on Thermal and Energy Management of a Fast-Charging Lithium-Ion Battery Pack with Air Cooling. *J. Energy Eng.* **2019**, *145*, 04019030. [CrossRef]
29. Xu, J.; Duan, Q.; Zhang, L.; Liu, Y.; Sun, J.; Wang, Q. The Enhanced Cooling Effect of Water Mist with Additives on Inhibiting Lithium Ion Battery Thermal Runaway. *J. Loss Prev. Process Ind.* **2022**, *77*, 104784. [CrossRef]
30. Zhao, R.; Liu, J.; Gu, J.; Zhai, L.; Ma, F. Experimental Study of a Direct Evaporative Cooling Approach for Li-Ion Battery Thermal Management. *Int. J. Energy Res.* **2020**, *44*, 6660–6673. [CrossRef]
31. Peng, W.; Zhang, Y.; Zhang, S.; Liu, X. Experimental Study on the Inhibition Effect of Water Mist Containing Additives on the Thermal Runaway of Lithium Battery. *Process Saf. Environ. Prot.* **2024**, *182*, 999–1007. [CrossRef]
32. Liu, T.; Tao, C.; Wang, X. Cooling Control Effect of Water Mist on Thermal Runaway Propagation in Lithium Ion Battery Modules. *Appl. Energy* **2020**, *267*, 115087. [CrossRef]
33. Liu, T.; Liu, Y.; Wang, X.; Kong, X.; Li, G. Cooling Control of Thermally-Induced Thermal Runaway in 18,650 Lithium Ion Battery with Water Mist. *Energy Convers. Manag.* **2019**, *199*, 111969. [CrossRef]
34. Das, L.; Pati, A.R.; Panda, A.; Munshi, B.; Sahoo, D.K.; Barik, K.; Mohapatra, S.S.; Sahoo, A. The Enhancement of Spray Cooling at Very High Initial Temperature by Using Dextrose Added Water. *Int. J. Heat Mass. Transf.* **2020**, *150*, 119311. [CrossRef]
35. Crafton, E.F.; Black, W.Z. Heat Transfer and Evaporation Rates of Small Liquid Droplets on Heated Horizontal Surfaces. *Int. J. Heat. Mass. Transf.* **2004**, *47*, 1187–1200. [CrossRef]
36. Wang, W.; He, S.; He, T.; You, T.; Parker, T.; Wang, Q. Suppression Behavior of Water Mist Containing Compound Additives on Lithium-Ion Batteries Fire. *Process Saf. Environ. Prot.* **2022**, *161*, 476–487. [CrossRef]
37. Zhang, T.; Liu, H.; Song, J.; Wang, B.; Wang, Y.; Shuai, X.; Guo, Z. Synergistic Inhibition Effect on Lithium-Ion Batteries during Thermal Runaway by N2-Twin-Fluid Liquid Mist. *Case Stud. Therm. Eng.* **2022**, *37*, 102269. [CrossRef]
38. Zhang, L.; Li, Y.; Duan, Q.; Chen, M.; Xu, J.; Zhao, C.; Sun, J.; Wang, Q. Experimental Study on the Synergistic Effect of Gas Extinguishing Agents and Water Mist on Suppressing Lithium-Ion Battery Fires. *J. Energy Storage* **2020**, *32*, 101801. [CrossRef]